JGR Space Physics

RESEARCH ARTICLE
10.1029/2022JA031158

Key Points:

- We estimated the atmospheric production rates of cosmogenic radionuclides using global geomagnetic field models covering the past 100 ka
- The results show the importance of the multipolar components of the field during the Laschamps excursion
- The variations in production rates predicted by the models agree well with the actual measurements from ice cores

Correspondence to:
S. Panovska,
sanja.panovska@gfz-potsdam.de

Citation:
Panovska, S., Poluianov, S., Gao, J., Korte, M., Mishev, A., Shprits, Y. Y., & Usoskin, I. (2023). Effects of global geomagnetic field variations over the past 100,000 years on cosmogenic radionuclide production rates in the Earth's atmosphere. *Journal of Geophysical Research: Space Physics*, *128*, e2022JA031158. https://doi.org/10.1029/2022JA031158

Received 16 NOV 2022
Accepted 17 JUL 2023

Effects of Global Geomagnetic Field Variations Over the Past 100,000 Years on Cosmogenic Radionuclide Production Rates in the Earth's Atmosphere

Sanja Panovska[1], Stepan Poluianov[2,3], Jiawei Gao[1,4,5], Monika Korte[1], Alexander Mishev[2,3], Yuri Y. Shprits[6,7,8], and Ilya Usoskin[2,3]

[1]GFZ German Research Centre for Geosciences, Section 2.3, Helmholtz Centre Potsdam, Potsdam, Germany, [2]Sodankylä Geophysical Observatory, University of Oulu, Oulu, Finland, [3]Space Physics and Astronomy Research Unit, University of Oulu, Oulu, Finland, [4]Institute of Geology and Geophysics, Chinese Academy of Sciences, Beijing, China, [5]College of Earth and Planetary Sciences, University of Chinese Academy of Sciences, Beijing, China, [6]GFZ German Research Centre for Geosciences, Section 2.7, Helmholtz Centre Potsdam, Potsdam, Germany, [7]Institute of Physics and Astronomy, University of Potsdam, Potsdam, Germany, [8]Department of Earth, Planetary, and Space Sciences, University of California, Los Angeles, CA, USA

Abstract The production rates of cosmogenic radionuclides, such as ^{10}Be, ^{14}C, and ^{36}Cl, in the Earth's atmosphere vary with the geomagnetic field and solar activity. For the first time, the production rates of several cosmogenic nuclides are estimated for the past 100 ka based on global, time-dependent geomagnetic field models and a moderate solar-activity level. In particular, the production rates were high with no notable latitudinal dependence during the Laschamps geomagnetic excursion (41 ka BP). The mean global production of ^{10}Be over the Laschamps excursion was more than two times greater than the present-day one, whereas the increase was 1.9 times for the Norwegian-Greenland Sea excursion (~65 ka), and only 1.3 times for the Mono Lake/Auckland excursion (~34 ka). All analyzed geomagnetic field models covering the past 100 ka, including the modern and Holocene epochs, lead to hemispheric asymmetry in the production rates, persistent overall time ranges, and reflected in the time-averaged nuclide production rates. Production rates predicted by the geomagnetic field models are in good agreement with actual measurements from ice cores and sediment records. These global, long-term production rates are important for a wide range of studies that employ cosmogenic nuclides as a proxy/tracer of different Earth system processes.

1. Introduction

It has long been recognized that the variations of the Earth's magnetic field contribute to significant changes in the production rates of cosmogenic radionuclides (e.g., Elsasser et al., 1956) through the modulation of the cosmic ray flux. These nuclides are produced in the atmosphere in a series of reactions caused by high-energy galactic cosmic rays (GCRs) (e.g., Beer et al., 2012; Lal & Peters, 1967). Assumptions that the geomagnetic field can be represented by a centered or eccentric dipole (e.g., Castagnoli & Lal, 1980; Nevalainen et al., 2013) are widely used in cosmogenic nuclide production rates (CNPRs) studies. Although this holds for a significant period of the geomagnetic field history when the field is dipole-dominated, events like geomagnetic excursions and reversals, when the field is highly non-dipolar, make clear exceptions. The effects of these transitional events on CNPRs have not yet been studied because the paleomagnetic field was mainly represented by dipole moment variations. Recent progress in long-term geomagnetic field reconstructions allows for studying the production rates considering data-based, global models over the past 100 ka and especially over geomagnetic excursions. Moreover, these global geomagnetic field reconstructions enable us to assess regional differences in CNPRs.

The main geomagnetic field exhibits spatial and temporal variations on a range of scales, days to centuries (e.g., Jackson & Finlay, 2015), centuries to millennia (e.g., Constable & Korte, 2015), and millions of years (e.g., Johnson & McFadden, 2015). Over geological timescales, the remanent magnetization in rocks and sediments provides a way of studying the past field beyond direct measurements. Our knowledge of the long-term changes in the geomagnetic field has greatly improved over the past two decades through modeling the field with paleomagnetic data. Several global, time-dependent models have become available covering the Holocene period (past ~12 ka) (e.g., Constable et al., 2016; Nilsson et al., 2022; Panovska et al., 2015; Pavón-Carrasco et al., 2014; Schanner et al., 2022; Usoskin et al., 2016). The geomagnetic excursions—periods when the field

intensity decreases and directions deviate significantly—have also been studied globally. The most recent events, the Mono Lake/Auckland (~34 ka) and Laschamps (~41 ka) are covered by a few models (Brown et al., 2018; Korte et al., 2019; Leonhardt et al., 2009) and their robust features are identified (Korte et al., 2019; Panovska et al., 2019). Moreover, continuous models for the past 70 ka (Panovska et al., 2021) and 100 ka (Panovska et al., 2018), which additionally include the Norwegian-Greenland Sea excursion (~65 ka), have been developed. The global models show extreme axial dipole (AD) decay during the Laschamps with a non-dipole field dominating at Earth's surface, and transitional field behavior observed globally (e.g., Panovska et al., 2021). The other two excursions are associated with a less pronounced drop of the AD moment and are not observed in directional data globally. They show evidence of being double events, that is a series of regional directional events associated with multiple dipole lows, rather than one global excursion (Korte et al., 2019; Panovska et al., 2021).

The cutoff in the cosmic ray (CR) rigidity (the ratio of a particle's momentum to charge) is often considered as a quantitative measure of the geomagnetic field shielding. It was first studied theoretically by Elsasser et al. (1956) and Størmer (1955), who provided equations of the cutoff rigidity as a function of the geomagnetic field dipole moment and geomagnetic latitude. A simplified approach is often used, where the values of cutoff rigidity are estimated analytically considering only the dipole field component (e.g., Usoskin et al., 2006). Eccentric dipole approximation is shown to be sufficient to represent the global features during times of dipole dominated field, but it may introduce moderate errors at regional scales (Nevalainen et al., 2013). Shea et al. (1965) estimated the cutoff rigidity by back-tracing trajectories of energetic particles in a given magnetic field, a method that has become a standard technique for modeling of the geomagnetic cutoff rigidity (e.g., Mishev et al., 2017; Smart et al., 2000). Over the Holocene timescale, this method has been applied to accommodate global paleomagnetic field models (e.g., Lifton et al., 2014, 2008). Beyond the Holocene, cutoff rigidities have been estimated using paleointensity stacks and AD moment reconstructions (e.g., Balco et al., 2008; Lifton et al., 2014). Recently, Gao et al. (2022a, 2022b) applied this method to the paleomagnetic field models spanning the past 100 ka and produced a synthesis record that represents the longest global reconstruction of geomagnetic cutoff rigidity.

Energetic CRs, when entering the Earth's atmosphere, initiate a complex nucleonic-electromagnetic-muon cascade, where in particular, some radioactive nuclides can be seldom produced. Since CRs are the main sources of these nuclides in the terrestrial system, they are called cosmogenic nuclides, and their abundance reflects the flux of CRs including its solar and geomagnetic modulation. A number of theoretical models for calculating the production rates of different cosmogenic nuclides in the Earth's atmosphere exist (e.g., Beer et al., 1990; Masarik & Beer, 2009; Poluianov et al., 2016, 2020). Considering the 100 ka time-dependent cutoff rigidity as one of the input parameters to these models, one can estimate the long-term production rates.

After production, some nuclides (e.g., ^{10}Be, ^{36}Cl) get transported in the atmosphere and finally deposited via wet or dry precipitation to land, ice, and sea, while other nuclides have different fates, for example, ^{14}C gets oxidized to $^{14}CO_2$, enters the carbon cycle and gets absorbed by living organisms, or ^{3}H is involved in the global water cycle. Thus, understanding their spatial and temporal variations is essential for a wide range of environmental and geological applications (e.g., Willenbring & von Blanckenburg, 2010), such as rates of Earth-surface processes, geochronology, and tracers of the atmospheric and hydrological circulation. Since the production rate has a nonlinear inverse relationship to the magnetic fields of the Earth and Sun (e.g., Kovaltsov et al., 2012; Masarik & Beer, 2009), cosmogenic nuclides are used to infer past variations of the geomagnetic field (e.g., Zheng et al., 2021), and of the solar activity, which in turn, is essential for studies of the solar-terrestrial relationship (e.g., Solanki et al., 2004; Steinhilber et al., 2012; Usoskin et al., 2021; Wu et al., 2018).

In this study, we modeled the influence of the internal geomagnetic field on atmospheric CNPRs due to GCRs. Recently developed, data-based, geomagnetic field models that cover long timescales are used to test the effects on different nuclides at different solar-modulation conditions. A range of available paleomagnetic field models makes it possible to extract the robust features and compare the results with numerical simulations and theoretical estimates of particle fluxes and CNPRs in the Earth's atmosphere. Further, the ^{10}Be estimates are compared to ^{10}Be deposition flux in the polar region as measured in the Greenland and Antarctic ice cores to validate the results of the calculation. First, we provide a short description of the methodology and the ingredients needed for calculating the production rates including paleomagnetic field models, cutoff rigidities, yield functions, CR spectrum, and solar modulation in Section 2. Section 3 includes the results regarding the geomagnetic excursions, effects of the solar modulation, different cosmogenic nuclides, average production over the past 100 ka, regional differences and hemispherical asymmetry, and tests against actual measurements by using a simple

parametrization of the deposition flux. We summarize the conclusions, discuss the implications of our estimates, and provide perspectives for future studies in Section 4.

2. Methodology

2.1. Paleomagnetic Field Models

Geomagnetic field variations on multi-millennial time scales are reconstructed using paleomagnetic data that come from archeological artifacts, volcanic rocks, and sediments. The Holocene period is covered by several global models, and large-scale variations are now well resolved (e.g., Nilsson et al., 2022; Schanner et al., 2022). Here, the Holocene period is represented by the CALS10k.2 model (Constable et al., 2016), constrained to a large extent by lake sediment records and archeomagnetic data, which dominate the most recent 3 ka. Recent efforts extend global geomagnetic field models on timescales beyond the Holocene (e.g., Panovska et al., 2019). Three global models are used in this study: LSMOD.2 (Korte et al., 2019), GGFSS70 (Panovska et al., 2021) and GGF100k (Panovska et al., 2018). All these models are based on sedimentary paleomagnetic records and to a lesser extent on volcanic data because of the very limited spatial and temporal distribution of the latter data set. The underlying sediment data sets differ in their spatial and temporal distribution, from an extensive data set of over 100 sediment records in the GGF100k model (100–0 ka) to a very limited data set of only nine sediment records selected with strict criteria in the GGFSS70 (70–15 ka), and regionally aligned and stacked sediment records in the LSMOD.2 (50–30 ka). These models are presented in spherical harmonics in space (up to degree 10, except the GGFSS70 model that goes to degree 6) and B-splines in time, including spatial and temporal regularization. Due to the limited data distributions, and measurement and age uncertainties, the effective spatial resolution is about degree 5 for the Holocene models, and degree 3-4 for the longer-duration models. Nevertheless, they have the advantage over geocentric dipolar approximations in providing dipole and non-dipole components of the field, with the latter being particularly important during the periods of geomagnetic excursions.

2.2. Cutoff Rigidity

The cutoff rigidity, that is, the geomagnetic field shielding, which is needed for estimating CNPRs, is calculated using the trajectory back-tracing method (e.g., Shea et al., 1965; Smart & Shea, 2009; Smart et al., 2000), where protons with a negative charge at a fixed rigidity are numerically traced back from the stratosphere (20 km above the Earth's surface) to space. If the proton can be traced back to the open space, this trajectory is considered as allowed; otherwise, the trajectory is forbidden (Cooke et al., 1991). The results of the simulations are parameterized via the effective vertical cutoff rigidity P_c so that all particles with the rigidity above/below P_c are considered as allowed/forbidden at a given location. Details on the method can be found in Gao et al. (2022a) and Smart et al. (2000).

The studies of Gao et al. (2022a, 2022b) provide global grids of the cutoff rigidity over the past 100 ka. Here, we use these recent results to calculate the corresponding changes in the CNPR pattern. The non-dipole components of the geomagnetic field during geomagnetic excursions are significant, and the trajectory-tracing method provides more realistic cutoff rigidities than the eccentric dipole approximation over periods of complex field morphology (Gao et al., 2022a). To reduce the calculation time and increase the accuracy in the lower rigidity interval expected for geomagnetic excursions, Gao et al. (2022a) introduced a hybrid rigidity scanning method in the trajectory-tracing technique. The first rigidity scan is from 30 to 0 GV with the 0.5 GV step, and the second rigidity scan is from the highest forbidden rigidity value plus 0.5 GV to the lowest allowed rigidity value minus 0.5 GV with the 0.01 GV step. By analyzing the cutoff rigidity from different models spanning the past 100 ka, Gao et al. (2022b) proposed a synthesis record (Rc100k) that can serve as a robust framework for the global 100 ka cutoff rigidity variability. For the purpose of analyzing, the robust characteristics and assessing models uncertainties, we considered the individual models that produced the Rc100k. However, it should be noted that even trajectory-tracing techniques can be inaccurate during geomagnetic excursions when the magnetospheric configuration is unknown; such periods require paleomagnetospheric models to be developed (e.g., Vogt & Glassmeier, 2001).

2.3. Solar Modulation

The flux of GCR near Earth is modulated by solar magnetic activity on time scales ranging from hourly/daily to centennial/millennial, including periods of Grand solar minima, when the Sun is very quiet (see Usoskin, 2023, for a review). Although the GCR modulation process is complex (Potgieter, 2013), it is often parameterized

for practical applications by a simple force-field approximation (Caballero-Lopez & Moraal, 2004; Usoskin et al., 2005), which includes a single modulation parameter ϕ in the units of rigidity and a prescribed local interstellar spectrum (LIS) of GCR. Here, we used the LIS as parameterized by Vos and Potgieter (2015). The use of other LIS shapes can slightly affect the exact value of ϕ which can be linearly converted to those obtained here (e.g., Asvestari et al., 2017; Usoskin et al., 2005), keeping thus the relative variability the same. The modulation parameter typically varies between 300 and 1,000–1,500 MV during a solar cycle and can be as low as 150–200 MV during Grand solar minima (Usoskin et al., 2021). On the other hand, on the multi-millennial time scale, the solar modulation can be considered roughly constant. The mean ϕ value over the period 1951–2016 was 660 ± 20 MV (Usoskin et al., 2017). The mid-late 20th century was characterized by very high solar activity, namely Modern Grand maximum (Solanki et al., 2004), when the mean modulation parameter was significantly higher than that during the Holocene $\phi = 449 \pm 70$ MV (Usoskin et al., 2016; Wu et al., 2018) as evaluated from cosmogenic proxy data. The mean modulation parameter was also estimated as $\phi = 496 \pm 40$ MV from lunar rock data on the million year timescale (Poluianov et al., 2018). Accordingly, we used the mean value of $\phi = 500$ MV for the estimates presented in this study, which is consistent with the periods of the last 10 thousand and 1 million years. We also used the range of ϕ from 0 to 2,000 MV to test the influence of different solar modulations (Section 3.2).

2.4. Modeling Cosmogenic Nuclide Production

We calculated the CNPRs in the Earth's atmosphere (noted as Q below) considering full Monte Carlo simulations of the nucleonic-muon-electromagnetic cascades caused by primary CRs as quantified by specific yield functions by Poluianov et al. (2016). This study provides altitudinal profiles of the production of five cosmogenic nuclides, ^{7}Be, ^{10}Be, ^{14}C, ^{22}Na, and ^{36}Cl, that are also analyzed here. The production rate $Q(h, t)$ in units of atoms/g/s at a given atmospheric depth h and time t can be computed as follows:

$$Q(h,t) = \sum_i \int_{P_c}^{\infty} Y_i(h,P) \cdot J_i(P,t) \cdot dP, \quad (1)$$

where P_c is the geomagnetic cutoff rigidity (Section 2.2), Y_i is the yield function that provides production of the given nuclide by the unit flux of primary cosmic ray particles of type i, rigidity P at atmospheric depth h, J_i is the rigidity spectrum of cosmic ray particles of type i near Earth, and the summation is over different types of cosmic ray particles, namely protons and α-particles. The α-particles effectively include heavier CRs with the scaling factor 0.353 in nucleonic number as obtained on the basis of the cosmic ray spectra directly measured by the AMS-02 experiment (Koldobskiy et al., 2019). The columnar CNPR is calculated as an integral of $Q(h, t)$ over atmospheric depth h and has units of atoms/cm^2/s.

Here, we use the cutoff rigidities estimated from the paleomagnetic field models (Gao et al., 2022a, 2022b), yield functions provided by Poluianov et al. (2016), the average GCR spectra calculated in the force-field approximation using the modulation potential $\phi = 500$ MV (see Section 2.3), and the LIS of CRs as provided by Vos and Potgieter (2015).

3. Results

To facilitate the presentation of the various aspects of CNPRs, we first considered one nuclide, namely ^{10}Be, and one model, LSMOD.2, that covers 20 ka. The period encompasses normal dipole-dominated and transitional fields, and together with varying solar modulation, will be used to demonstrate their effects on the production rates. To illustrate the overall consistency of the results obtained for ^{10}Be with other nuclides, analyses of ^{7}Be, ^{14}C, ^{22}Na, and ^{36}Cl are also presented. Then we come to the 100 ka period and assess robust features, the model's variability and uncertainty.

3.1. The Effect of Geomagnetic Excursions

We looked at the long-term production separately as a function of the geomagnetic field and solar modulation (Section 3.2). The columnar production over the globe of three epochs from the LSMOD.2 model are shown in Figure 1 for ^{10}Be. The selected epochs correspond to a high dipole moment (7.8×10^{22} Am^2) at 47.15 ka

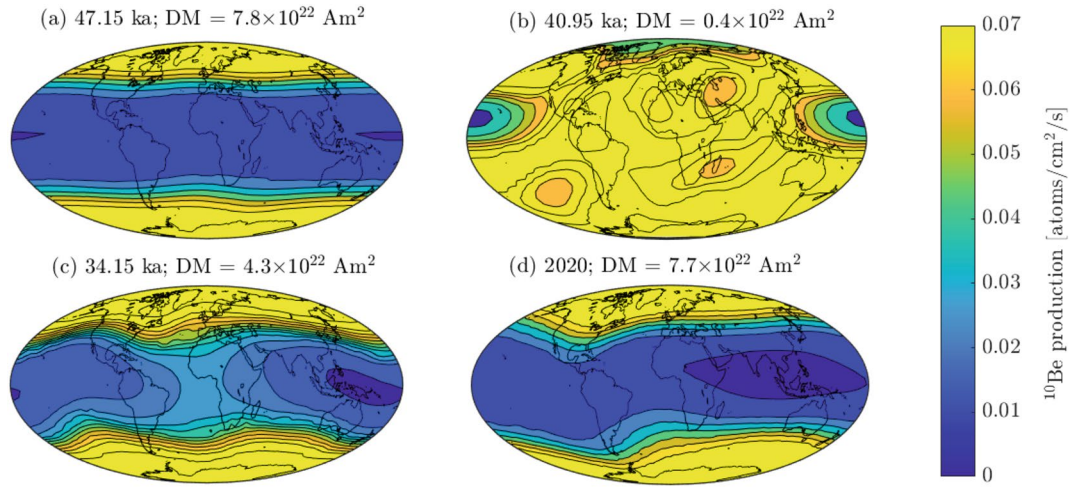

Figure 1. Columnar production of ^{10}Be estimated from the LSMOD.2 model (a–c), and IGRF13 (d) for comparison with the present-day production. The solar modulation potential ϕ is 500 MV. All maps are plotted on the same color scale. Selected example epochs correspond to a high dipole moment at 47.15 ka (a), the Laschamps excursion at 40.95 ka (b), Mono Lake/Auckland excursion at 34.15 ka (c), and the present-day 2020 (d). Dipole moment (DM) variation of the LSMOD.2 model and selected epochs are presented in Figure 3a.

(Figure 1a), the Laschamps excursion at 40.95 ka with the dipole moment of 0.4×10^{22} Am^2 (Figure 1b), the Mono Lake/Auckland excursion at 34.15 ka, with the dipole moment of 4.3×10^{22} Am^2 (Figure 1c), and IGRF13 (Alken et al., 2021) (Figure 1d) for comparison with the present-day production (the dipole moment is 7.7×10^{22} Am^2). Figures 2a–2d show the latitudinal profiles of the computed ^{10}Be production rates for the four epochs. The

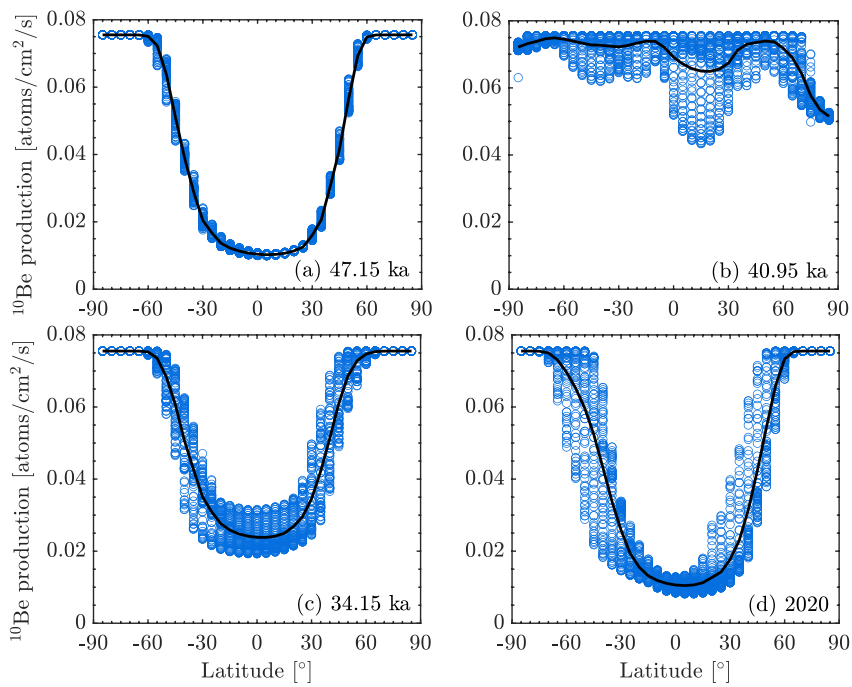

Figure 2. Columnar production of ^{10}Be estimated from the LSMOD.2 model (a–c), and IGRF13 (d) for comparison with the present-day production. Plots show the production at the given epoch as a function of latitude (blue circles, corresponding to different longitudes) and the average (black line). The solar modulation potential ϕ is 500 MV. All plots have the same y-axis. Selected example epochs correspond to a high dipole moment at 47.15 ka (a), the Laschamps excursion at 40.95 ka (b), Mono Lake/Auckland excursion at 34.15 ka (c), and the present-day 2020 (d). Maps of cosmogenic nuclide production rates for the selected epochs are presented in Figure 1.

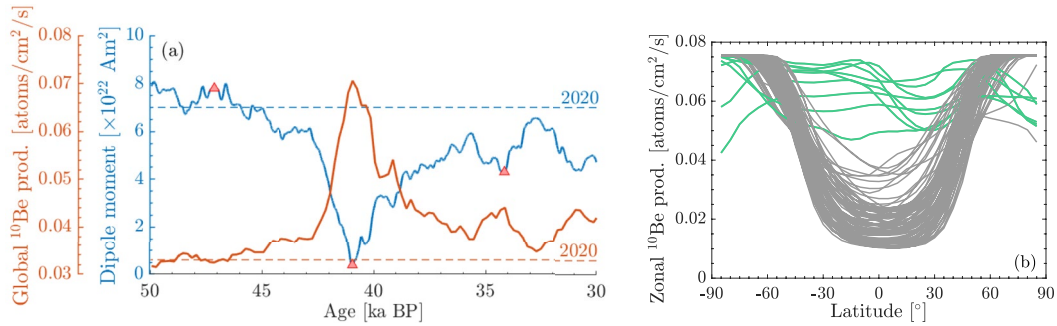

Figure 3. Summary of LSMOD.2 model variations: (a) dipole moment and the global mean production of ^{10}Be, $\phi = 500$ MV (blue and red curve, respectively). Dashed lines denote the present-day dipole moment (year 2020) and ^{10}Be global production estimated from the IGRF13 model. Selected epochs presented in Figure 1 are denoted with red triangles. (b) Mean zonal production over the model validity period 50–30 ka at time step of 200 years. The green lines associated with the Laschamps excursion over the period 40.15–41.75 ka do not show systematic latitudinal dependence.

global CNPR of ^{10}Be over the period of 50–30 ka ago is shown in Figure 3a along with the dipole-moment variations according to the LSMOD.2 model. The present-day columnar ^{10}Be production rate is 5-6 times higher at high latitudes than in the equatorial region (cf. Poluianov et al., 2016) whereas, during the periods of geomagnetic excursions, the production pattern depends on the exact geomagnetic field configuration. Over the Mono Lake/Auckland excursion (Figures 1c and 2c), when the dipole moment is approximately half of the present-day, the dipole production pattern is still present, but with a reduced difference (ca. a factor of three) between polar and tropical regions. The latitudinal structure is clearly present in Figure 2c as in the periods of high dipole moment (Figures 2a and 2d). No latitudinal structure and almost equal, high production rates everywhere are observed during the extreme case at 40.95 ka, the Laschamps excursion, when the dipole moment was only 5% of the modern field (Figure 1b). The production rates are globally comparable to the present-day polar productions, with small, irregularly distributed regions of slightly decreased production that reflect the high-order, non-dipolar morphology of the geomagnetic field during the Laschamps (Figure 2b). The production in polar regions can be higher, but also lower compared to other latitudes, depending on the specific distribution of the magnetic field as, for example, in the case for this particular epoch with decreased production in the northern polar region (Figures 1b and 2b). In terms of the dipole approximation, the geomagnetic dipole was estimated to be nearly perfectly centered and axially aligned with the rotational axis leading to no longitudinal patterns in the CNPR distribution, observed as a very narrow spread of individual points along the mean curve in Figure 2a at 47.15 ka. On the contrary, the spread is broad in Figure 2d, because of the essential displacement and tilt of the present-day dipole with respect to the Earth's center and rotational axis, respectively. The equatorial dip becomes shallower with the decrease of the dipole moment during the Mono Lake/Auckland event (Figure 2c).

The global average CNPR is inversely related to the geomagnetic dipole moment, with peaks in production corresponding to lows in the geomagnetic field intensity (Figure 3a). The mean global production over the Laschamps excursion is more than double the present-day one, whereas the increase is only 1.3 times of the present-day production for the Mono Lake/Auckland excursion, considering the two intensity lows of this excursions, at ∼34 and ∼31 ka (e.g., Korte et al., 2019).

A summary of zonal mean production profiles over the whole 50–30 ka period with the 200 years step is provided in Figure 3b. The green lines mark the production during the Laschamps excursion between 40.15 and 41.75 ka ago, and they do not show any systematic latitudinal dependence. This period with a duration of 1.6 ka, when the dipole moment was less than 40% of the present-day value, agrees well with the estimated global surface duration of the Laschamps excursion (e.g., Korte et al., 2019; Panovska et al., 2021).

Figure 4 depicts the ^{10}Be CNPRs in the atmospheric column as a function of latitude (longitude is fixed to zero) for the three selected epochs and the present-day. One can see differences in CNPR patterns during different epochs. Latitudinal structure and maximum production in the polar regions can be observed at 47.15 ka and the modern epoch (Figures 4a and 4d) and to some extent at 34.15 ka ago (Figure 4c), in contrast to the Laschamps event characterized by no latitudinal dependence and nearly homogeneous production rate (Figure 4b). Also noticeable is the higher production in the Southern Hemisphere compared to the northern (Figures 4a and 4d).

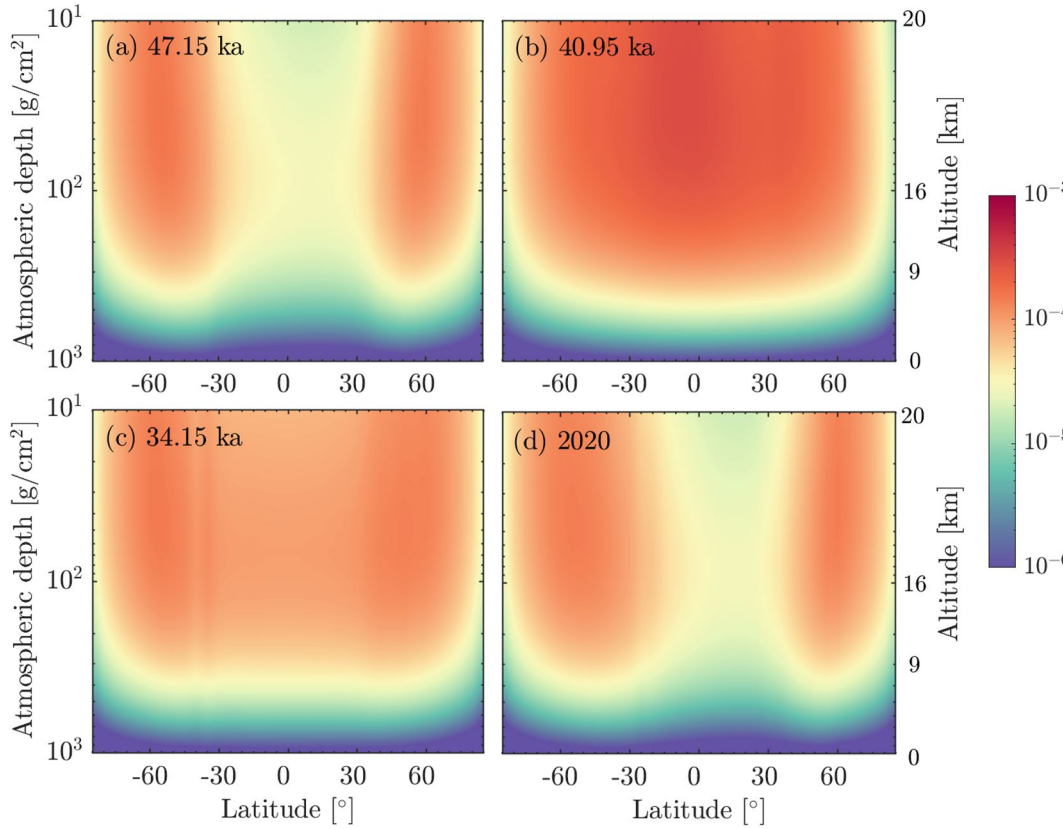

Figure 4. Production of ^{10}Be (in units of atoms/g/s) estimated from the LSMOD.2 model at 47.15 ka (a), 40.95 ka (b), 34.15 ka (c), and the IGRF13 model at 2020 (d) in the atmospheric column as a function of latitude caused by galactic cosmic rays. Each cell is latitudinally weighted, that is multiplied by cosine(latitude). Longitude is fixed to 0°. The solar modulation ϕ is 500 MV. All plots have the same color scale and axes. The altitude is given in depth (g/cm^2) on the left *y*-axis, and approx. height in km on the right *y*-axis using the U.S. Standard Atmosphere (National Oceanic and Atmospheric Administration, 1976) for the conversion.

3.2. The Effect of Solar Modulation

The global CNPR varies by ±20%–25% during a typical solar cycle because of the solar modulation of GCR (e.g., Heikkilä et al., 2008; Kovaltsov & Usoskin, 2010). However, these modulation values can change depending on the global morphology of the geomagnetic field. Here, we looked at the global ^{10}Be production for a range of solar modulations from 0 to 2,000 MV, at 250 MV step, and different geomagnetic field configurations for the selected epochs (Figure 5a) as well as the temporal variations over the period of 50–30 ka ago using the LSMOD.2 model (Figure 5b). The $\phi = 0$ would imply the total absence of the solar modulation, which is a non-realistic situation because the modulation is known to exist even during the Grand solar minima although at a low level of 100–200 MV (Poluianov et al., 2014; Wu et al., 2018). These estimates show that the global average production significantly changes depending on solar modulation. The production nonlinearly increases with decreasing the solar modulation, and the effect becomes stronger for weaker geomagnetic shielding. The global production rate during the Laschamps excursion (red curve in Figure 5a) is estimated to be more than doubled relative to the present-day values (dotted magenta curve). The increase during the Mono Lake/Auckland excursion (yellow curve) is smaller than that for the Laschamps event, but still significant, of the order of about 33% for almost the entire range of the solar modulation parameter. This effect can also be seen in Figure 5b (see the large range of variations around 41 ka). For large values of the solar modulation (lower lines in Figure 5b), the effect of geomagnetic field is highly suppressed, that is, production rates are less sensitive to geomagnetic field variations.

We combined the variations in the global production rates of ^{10}Be that result from changes in solar modulation ranging from 0 MV (no solar modulation) to 2,000 MV (very active Sun) and with fluctuations in the geomagnetic

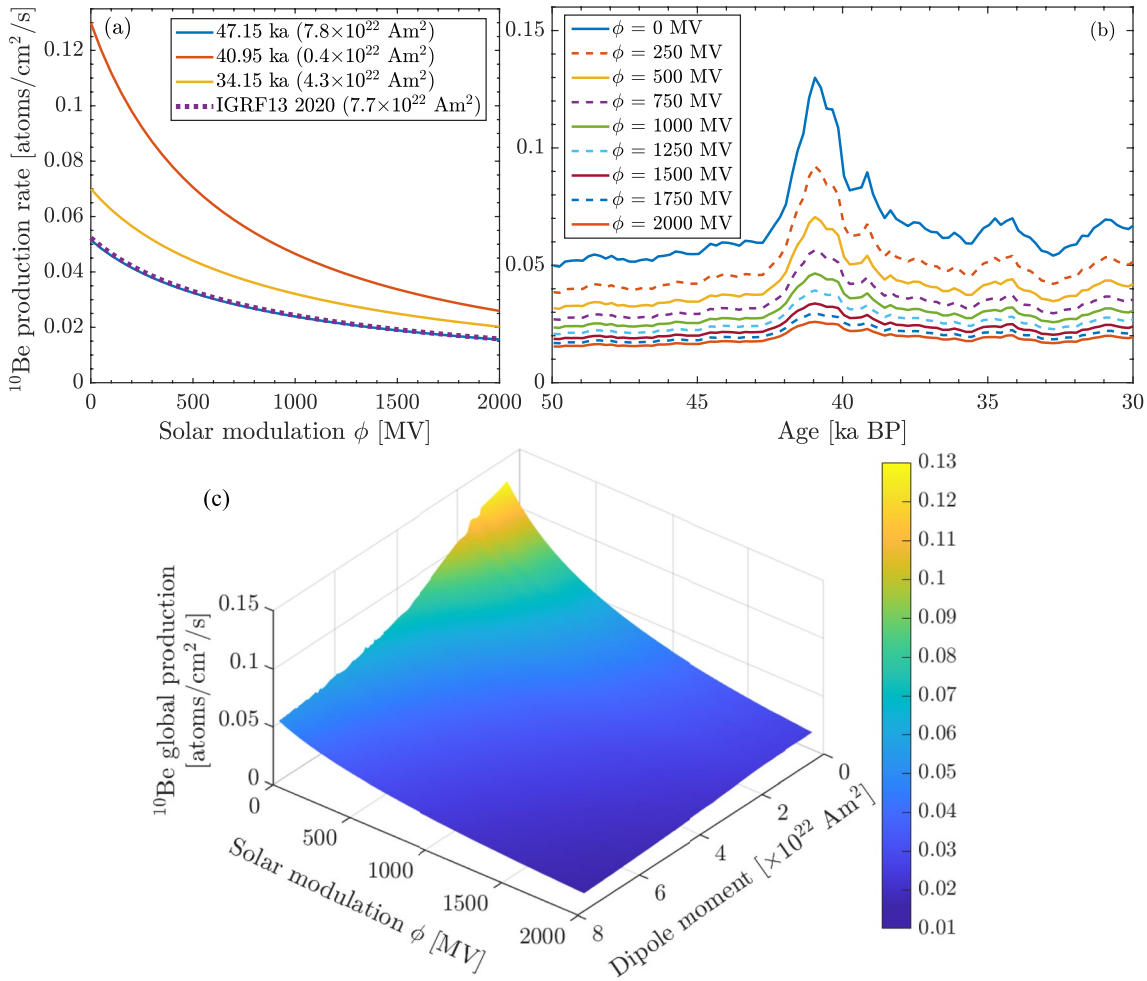

Figure 5. (a) Mean global production rates of ^{10}Be as a function of the solar modulation ϕ from the LSMOD.2 model for different values of the dipole moment, provided in the brackets in the legend. IGRF13 model values are plotted for comparison purposes. Same epochs as in Figure 1 are selected. (b) Time variations of the mean global production rates of ^{10}Be from the LSMOD.2 model for different values of the solar modulation potential ϕ ranging from 0 to 2,000 MV at 250 MV step. (c) Global production of ^{10}Be estimated from the LSMOD.2 model as a function of the dipole moment and the solar modulation. Estimates have been interpolated using 2D cubic interpolation for plotting the surface.

field, expressed in dipole moment values, from almost 0–8 × 10^{22} Am^2 in Figure 5c. For the latter, we estimated mean production rates based on the LSMOD.2 global variations. This dependence on both heliospheric and geomagnetic modulations is often analyzed from Monte Carlo calculations (e.g., Masarik & Beer, 1999, 2009), assuming dipolar Earth's magnetic field and shielding effects dependent on the geomagnetic latitude. Here, the estimates are based on the global morphology of the geomagnetic field from the LSMOD.2 model. At first glance, the dependence is as expected, meaning peak/increased production when the shielding of both fields is absent/low.

However, the geomagnetic-field shielding differs depending on the approximation used, be it an AD, geocentric tilted dipole, or the full model representation. Figure 6 shows the comparison of ^{10}Be production rates for a given solar modulation parameter (ϕ = 500 MV) as a function of the geomagnetic field based on the LSMOD.2 paleomagnetic field model truncated at different levels: the AD only, degree 1 (the geocentric tilted dipole), degrees 3 and 5. The model has fewer points with very low dipole moment, because, for most of the period the model covers, the geomagnetic field is high. All the curves (Figures 6a and 6b) agree well for geomagnetic field values close to 1 (present-day) but start to disperse at about 50% of the present-day value. As expected, the effect of the non-(axial) dipole components is most prominent during the Laschamps excursion, where the AD and dipole overestimate the mean production rates. In general, the mean production obtained from the model truncated at degree 5 is very close to the full representation (degree 10), which points to the effective spatial resolution of

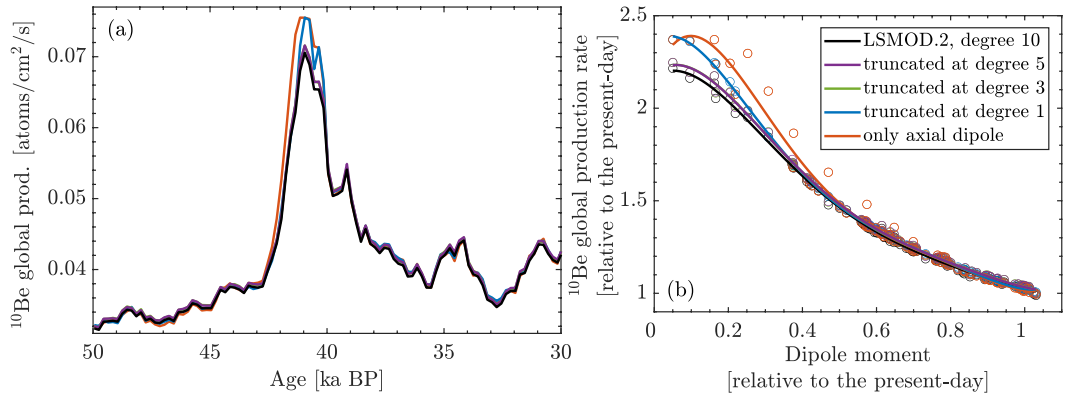

Figure 6. (a) Time variations of the global average production rates of ^{10}Be with the geomagnetic field taken from the LSMOD.2 model. Different levels of truncation are considered for assessing the influence of non-axial dipole and non-dipole components on the production rates. The solar modulation parameter for all the estimates is 500 MV. The same legend applies to both subplots. (b) Global average production of ^{10}Be as a function of the dipole moment. Circles are global mean production rates estimated at time steps of 200 years. Polynomial of degree 5 is applied to fit the production rates of the model. The dipole moment obtained from this geomagnetic field model goes slightly above the modern-day value. Dipole moment and mean ^{10}Be production rate are expressed relative to the present-day values, that is, the 2020 values from the IGRF13 model, 7.7×10^{22} Am^2 and 0.03185 atoms/cm^2/s, respectively. The curves representing the truncation levels 3 and 5 are practically indistinguishable in both plots.

this model to about spherical harmonic degree 5 (Korte et al., 2019). Although the mean global production for the full expansion and different truncation levels agree when the dipole moment is high, regional differences still exist. In general, the AD assumption overestimates the production over periods of low dipole moment but underestimates the production at high dipole moments (see, for instance, the period 48–44 ka in Figure 6a, where the AD estimates are slightly lower than the full model, opposite to the effect observed over the Laschamps excursion). However, the underestimation is not significant considering the uncertainties in the models. The difference in ^{10}Be global mean production rates between the geomagnetic field model and its truncation to the AD and dipole is about 18% and 10%, respectively, over the period of low dipole moment (10%–20% of the present-day, that is, 0.1–0.2 in the *x*-axis in Figure 6b).

3.3. Production Over the Past 100 ka

Regarding the time variations of ^{10}Be production rates over the past 100 ka, we considered all global models available on these timescales and analyzed the mean global production, as well as the Northern versus Southern Hemisphere production rates (Figure 7). Using different models instead of the Rc100k combined record will allow an assessment of robust features and give an idea of models' variability and uncertainty over periods when the different models overlap. The average global production rate is 0.0353 atoms/cm^2/s over the past 100 ka, 0.0420 atoms/cm^2/s over 70–15 ka, 0.0412 atoms/cm^2/s for the 50–30 ka, and 0.0311 atoms/cm^2/s over the Holocene. Compared to estimates from numerical simulations, the 100 ka and Holocene values are close together and in fair agreement with the Holocene average of 0.0346 atoms/cm^2/s estimated by Heikkilä and von Blanckenburg (2015). We note that the latter results were based on an outdated nuclide-production model and maybe uncertain by 20%–30% (Golubenko et al., 2022). Increased mean production rates obtained from the LSMOD.2 and GGFSS70 models partly result from the periods of geomagnetic excursions and lower dipole moment compared to the more strongly dipolar periods covered by the CALS10k.2 and IGRF model. The GGF100k model average lies between the other two sets of models, due to its greater smoothing over longer time spans, including excursions, and dipole moment that is not as low as in the other two models. The "Laschamps run", zero geomagnetic dipole test of the Heikkilä et al. (2009) simulation predicts 0.0524 atoms/cm^2/s, but the results presented here as based on paleomagnetic field models give somewhat higher values over the Laschamps, 0.0748 and 0.0706 atoms/cm^2/s, from the GGFSS70 and LSMOD.2 models respectively. The discrepancy results not only from the paleomagnetic models but also from the different production models. The values are also higher than the production values of 0.0621 ± 0.0060 atoms/cm^2/s and 0.0638 ± 0.0112 atoms/cm^2/s obtained from sediment stacks of ^{10}Be over the Laschamps excursion and the Matuyama-Brunhes reversal (Simon et al., 2018, 2020), respectively, using the

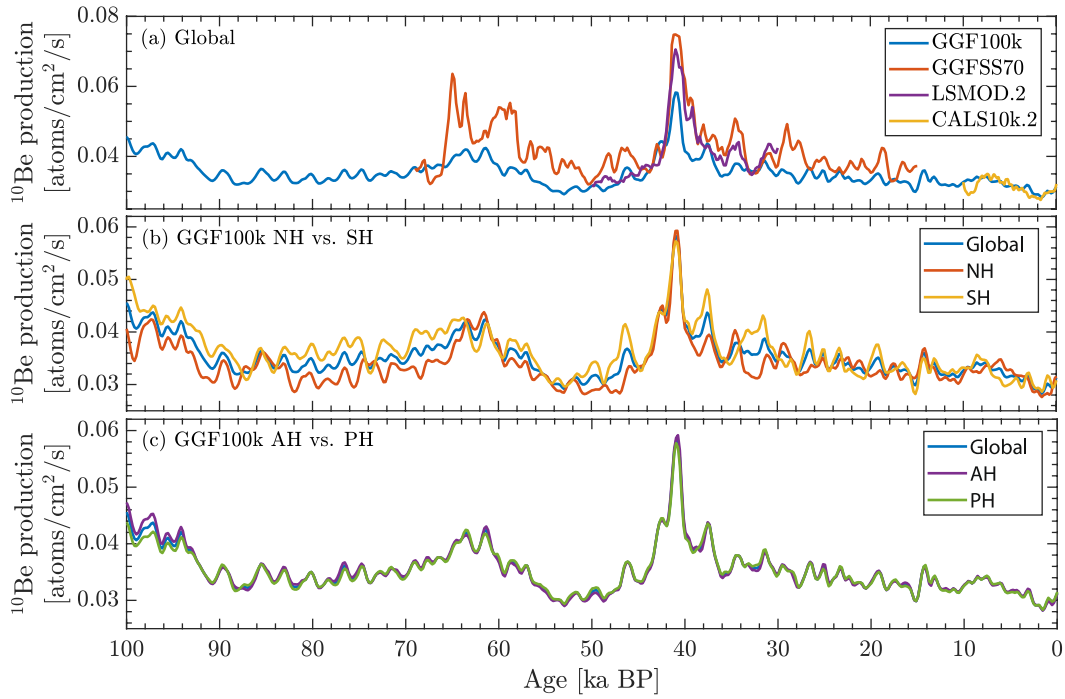

Figure 7. Global production of ^{10}Be over the past 100 ka modeled using the following paleomagnetic field models: GGF100k, GGFSS70, LSMOD.2, and CALS10k.2 (a). References are in the main text. The solar modulation potential ϕ is 500 MV. The longest 100 ka model is used to demonstrate the hemispherical asymmetry in the ^{10}Be production: Northern versus Southern Hemisphere (NH vs. SH) in (b) and Atlantic versus Pacific Hemisphere (AH vs. PH) in (c).

same theoretical ^{10}Be production model of Poluianov et al. (2016). Increased mean production is predicted at other periods of low field intensity (Figure 7a), 0.0636 atoms/cm^2/s at the Norwegian Greenland Sea excursion (~65 ka), and 0.0508 atoms/cm^2/s at the Mono Lake/Auckland excursion (~34 ka).

The latitudinal asymmetry has also been observed in the geomagnetic secular variation on different time scales (e.g., Aubert et al., 2013; Constable et al., 2016). We calculated the average hemispheric production of ^{10}Be to assess if this asymmetry is reflected in the production estimates. Figures 7b and 7c present the Northern, Southern, Atlantic, and Pacific Hemisphere mean productions based on the model GGF100k. The boundaries of the latter two are set at the meridians 90°W and 90°E. A summary of the global and hemispheric mean productions of all analyzed models is provided in Figure 8. All models, which sample a large range of timescales—from modern to 100 ka-average show the Northern/Southern asymmetry in the production rates due to stronger, on

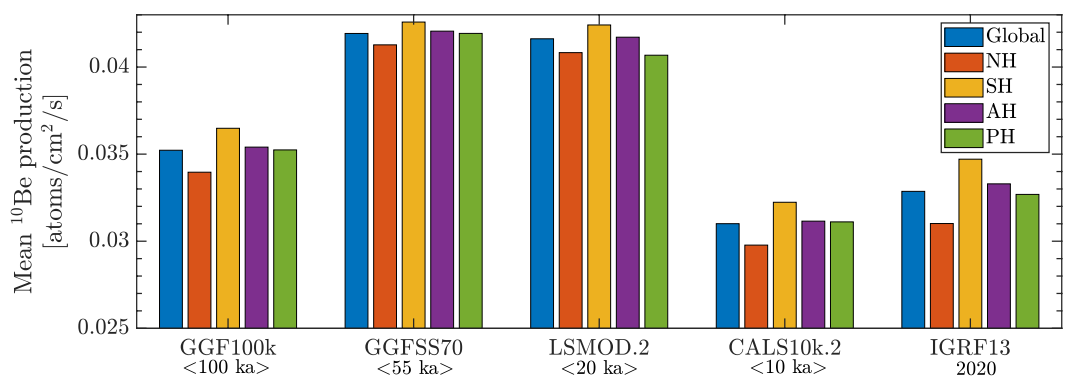

Figure 8. Differences in the global and hemispherical production of ^{10}Be over the past 100 ka for different paleomagnetic field models: GGF100k (100–0 ka BP), GGFSS70 (70–15 ka BP), LSMOD.2 (50–30 ka BP), CALS10k.2 (10–0 ka BP), and IGRF13 estimates for year 2020. The solar modulation potential ϕ is 500 MV. NH, Northern Hemisphere; SH, Southern Hemisphere; AH, Atlantic Hemisphere; and PH, Pacific Hemisphere.

average, field in the Northern than in the Southern Hemispheres. On the other hand, no asymmetry is evident in the Atlantic and Pacific Hemispheric mean production rates. In the Southern Hemisphere, the global mean production is larger for all time scales, 92% of the Holocene period (result from the CALS10k.2 model), ~60% of the time in the LSMOD.2 and GGFSS70 models, and 75% in the GGF100k, considering the models' validity periods. However, the asymmetry is not that clear during the excursional midpoints when the production rates are at the maximum level globally. The difference in the average field strength in the Southern versus Northern Hemisphere is mainly related to the influence of significant average axial quadrupole contribution (g_2^0) in the geomagnetic field overall analyzed timescales, up to 100 ka (Constable et al., 2016; Panovska et al., 2019). The numbers are comparable to the time-averaged values over million years scales (e.g., Johnson & McFadden, 2015). Therefore, we tested if the North/South asymmetry is present when the geomagnetic field model is truncated to the first four Gauss coefficients. For that reason, we considered the dipole (g_1^0, g_1^1, and h_1^1) and axial quadrupole (g_2^0) terms from the LSMOD.2 model for calculating the cutoff rigidity. These values are then used to obtain the global ^{10}Be production rate estimates. The hemispherical asymmetry observed in the full models exists in the case of truncated model, indicating the importance of the axial quadrupole contribution to the field asymmetry.

The values of CNPRs reported here, describing the effects of paleomagnetic field models, come with uncertainties related to these models. Propagating the uncertainties from the geomagnetic field to cutoff rigidities and production rates is not straightforward. We used the upper and lower bounds of cutoff rigidity of the GGF100k provided by Gao et al. (2022b) to assess the uncertainties in production rates. When comparing the global averages, the percentage difference is 1%–2% for strong, dipole-dominated epochs and 3%–4% for weaker field and excursion epochs. These are significantly lower than the 20% deviation estimated from the dipole model approximation. Nevertheless, these uncertainties come from one model only and are probably underestimated. The more realistic uncertainties are the order of differences between different models. The global averages of LSMOD.2, GGFSS70, and GGF100k, considering the ^{10}Be and the overlapping period 50–30 ka, differ by 8%–14%.

3.4. Production of Other Cosmogenic Nuclides

Many studies based on cosmogenic nuclides employ nuclides other than the ^{10}Be. Poluianov et al. (2016) provided the yield functions of four other cosmogenic nuclides, ^{7}Be, ^{14}C, ^{22}Na, and ^{36}Cl, and we have also estimated their global production-rate patterns (Figure 9). Maps in Figure 9 present distributions of the columnar production rates at the same epochs as in Figure 1 for ^{10}Be. The absolute values of the production rates differ by orders of magnitude between nuclides so that the production rates are higher for ^{7}Be and ^{14}C produced on abundant nitrogen and oxygen, and lower for ^{22}Na and ^{36}Cl produced by spallation of less abundant argon. However, the spatial distribution of the production rates remains qualitatively similar to that discussed for ^{10}Be (Section 3.1). Also, the production rates reported previously by using the LSMOD.2 model are in very good agreement with the results from the other analyzed paleomagnetic field models (Section 3.3), and also confirmed with the analysis of different cosmogenic nuclides.

3.5. Comparison With Actual Measurements

In this section, we validate the obtained results by comparing the modeled ^{10}Be to actual measurements. We computed the depositional flux of ^{10}Be flux in the Northern and Southern polar regions and checked the agreement with the measured values in Greenland and Antarctic ice cores, as shown in Figure 10. In addition, we have also compared the global production of ^{14}C with the IntCal20-based ^{14}C production rates (Köhler et al., 2022) in Figure 10d. Having the nuclide atmospheric production calculated over the whole atmospheric depth and time span of the models, we applied a simple deposition model to calculate the deposition flux in the northern polar region (60°N–90°N). We used the parametrization provided in Heikkilä et al. (2009) and kept in mind the uncertainties of a modern-era model used in conditions over many millennia in the past. The mean solar modulation parameter is taken as 500 MV. Looking at the polar latitudes, the production-deposition is as follows: 2% of ^{10}Be produced in the stratosphere, 19% of nuclides produced in the troposphere latitudinal range 60°–90°N, and 5% from the troposphere 30°–60°N range (Heikkilä et al., 2009). On the other hand, over the Laschamps excursion, the values are 3%, 27%, and 6%, respectively, and additionally about 1% from the 0°–30°N range of the troposphere. We considered the Laschamps run for the period 44–38 ka, the actual Laschamps excursion (see the inset plot in Figure 10). The tropopause is derived from the JRA55 reanalysis that was provided as zonal monthly means for the period 1960–2018 (Pisoft et al., 2021) because this data set has the advantage of

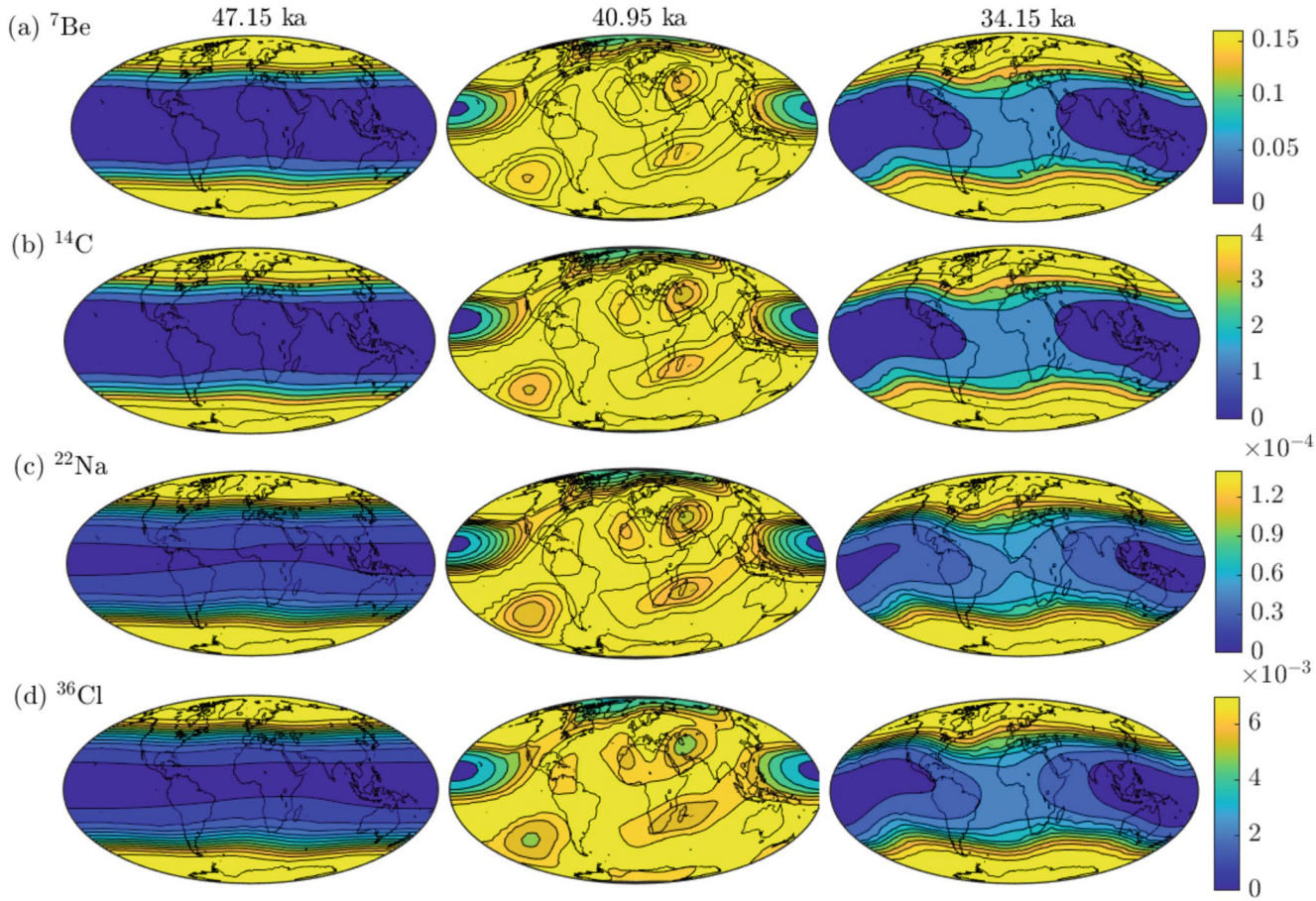

Figure 9. Global pattern of the columnar production rates of ^{7}Be (a), ^{14}C (b), ^{22}Na (c), and ^{36}Cl (d) presented in rows, for different epochs from the LSMOD.2 model (ordered by columns): high dipole moment at 47.15 ka, the Laschamps excursion at 40.95 ka, and Mono Lake/Auckland excursion at 34.15 ka. The solar modulation ϕ is set to 500 MV. The color scales represent the production rate in atoms/cm^2/s. They are different for different nuclides.

using longer time series. For approximating the average tropopause better, the profiles that were not realistically simulated over the southern polar regions due to active winter vortex, low temperatures, and indifferent vertical profiles, were not considered when estimating the average. The mean latitudinal profile of the tropopause has a variable height and ranges between ∼9 km in the polar region to ∼16 km above the equator. Accordingly, the parametrization provided in Heikkilä et al. (2009) for the southern polar region (60°S–90°S) and the Laschamps run are considered for the comparison with the Antarctic ice core data. However, it should be understood that the present-day warm-climate tropopause may not be applicable for the ice-age condition leaving the presented result only indicative.

The ^{10}Be measurements from the Greenland ice cores GRIP and GISP2 (Muscheler et al., 2004) combined, using the updated GICC05 time scale, are in good agreement with the calculated ^{10}Be flux (Figure 10). Although the most common approach is to study the relative production rate variations, we opt here for keeping the absolute scale for illustrating the comparison. In general, the GGFSS70 model predicts the flux well within the data scatter except for parts of the period 27–15 ka ago when it is systemically lower. This short discrepancy may be due to reasons such as poorly resolved paleomagnetic field models, imprecise ice-core flux estimates during Marine Isotope Stage 2 (29–14 ka), or to potential climatic signals in the ^{10}Be record in ice. The GGF100k model yields smoother results, and deposited fluxes which are systematically lower than the other models as a result of the higher dipole moment of GGF100k over the whole time span. The Laschamps excursion is clearly characterized by an increased flux with all the models, though the amplitude in all models is smaller than the measured flux. When considering the parametrization of the Laschamps run from Heikkilä et al. (2009), the predicted flux increase is larger than in our models so that it matches the observed one for the Laschamps excursion but overestimates the flux during the other times. The ice cores EDC, EDML, and Vostok from Antarctica (Adolphi et al., 2018;

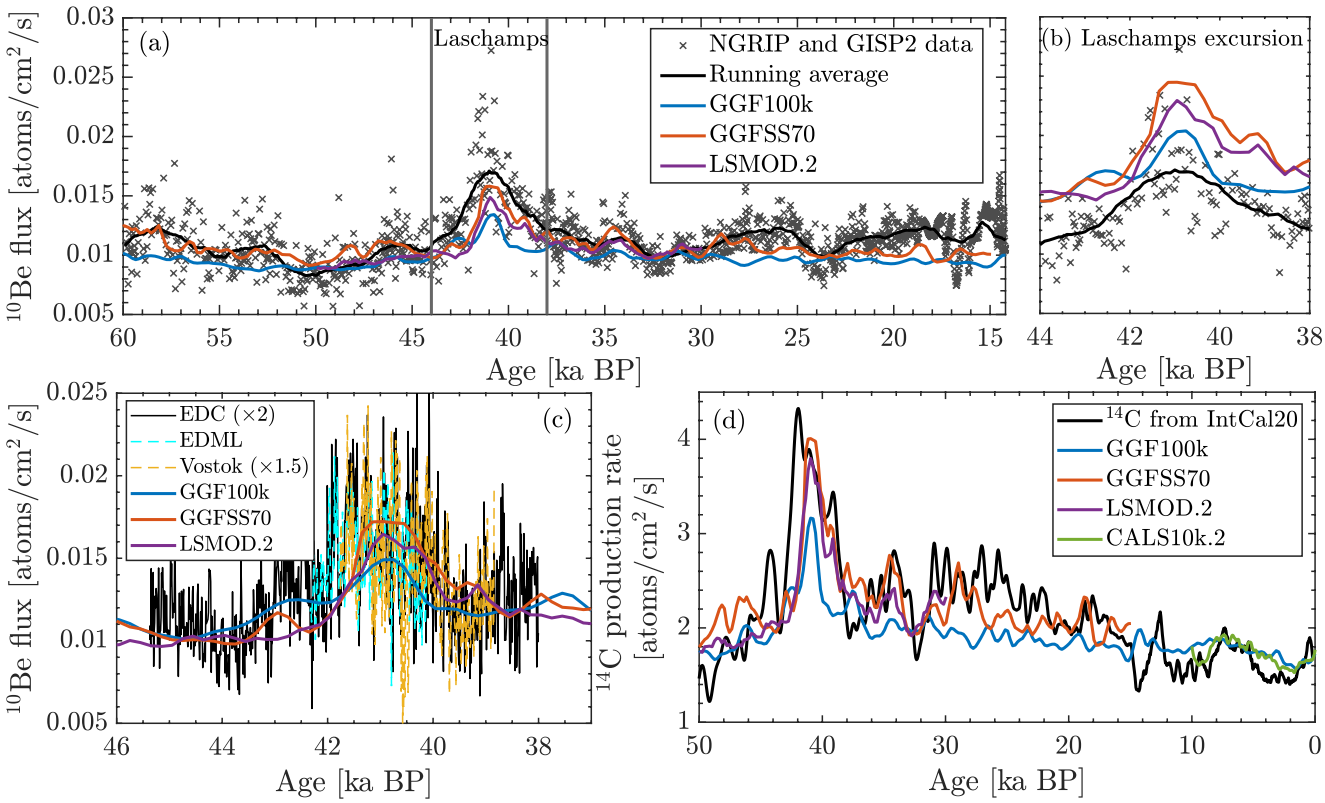

Figure 10. (a) Comparison of the deposition flux of ^{10}Be in the polar region (60°N–90°N) using the presented production estimates from the long-term geomagnetic field models and measured data from the Greenland ice cores GRIP and GISP2 combined (Muscheler et al., 2004). The Greenland data (cross symbols) are plotted on the updated GICC05 time scale. The solid black line represents 1,000 year running means with a sliding window of 100 years. The solar modulation potential ϕ is 500 MV. The atmospheric transport was parameterized according to Heikkilä et al. (2009). (b) Comparison over the period of the Laschamps excursion. The atmospheric transport is based on the parameters of the Laschamps run in Heikkilä et al. (2009). (c) Comparison of the deposition flux of ^{10}Be in the southern polar region (60°S–90°S) and measured data from the Antarctic ice cores EDC, EDML, and Vostok (Adolphi et al., 2018; Raisbeck et al., 2017). (d) Comparison with IntCal20-based ^{14}C production rates in the atmosphere (Köhler et al., 2022, scenario V1).

Raisbeck et al., 2017) are short and cover only the Laschamps excursion. The modeled variations are smoother, and though they capture the Laschamps' peak, the period of increased production is slightly wider in the measured records (Figure 10c). The IntCal20-based ^{14}C production in the atmosphere (Köhler et al., 2022, scenario V1, 50–0 ka) and modeled values show a good agreement in the general trend, but the small-scale features require more work, both on the paleomagnetic field models and processes in the carbon cycle (Figure 10d). Nevertheless, good agreement between the flux variations measured in the ice cores and ^{14}C production rates, and the estimated ones supports the approach used.

4. Conclusion

Evidence for increased production of cosmogenic nuclides during periods of the decreased geomagnetic field intensity has been found in many studies of sediment and ice cores (e.g., Bourlès et al., 1989; Carcaillet et al., 2004; Christl et al., 2010; Frank et al., 1997; Simon et al., 2020, 2016), but the nuclide production rates using data-based, global paleomagnetic field models have not been estimated previously. Available long-term global models, presently spanning up to 100 ka, are employed here to estimate possible effects of the internal geomagnetic field variations on CNPRs, with the special attention to geomagnetic excursions. The production rates computed for periods with stable, dipole-dominated geomagnetic field strongly depend on the geographical latitude, whereas the production rates during the Laschamps excursion are roughly constant at all latitudes, with slight differences depending on the global geomagnetic field morphology. The other regional excursions show reduced latitudinal dependence relative to strongly dipolar fields. Considering only the (axial) dipole in the cutoff rigidity estimates can lead to an overestimation of the production for periods of low magnetic field intensity.

When more global models of excursions and reversals become available, they may be used to test and validate the results presented here.

The global average CNPRs during different excursions over the past 100 ka period increase significantly above the present-day value, by a factor of 1.5 for the Mono Lake/Auckland event, 1.9 for the Norwegian-Greenland Sea excursion, and 2.3 for the Laschamps excursion, considering ^{10}Be and GGFSS70 model. The modeled increases of the production rate during geomagnetic excursions appear robust for all the studied nuclides and paleomagnetic field models. For instance, the increase obtained for the Laschamps excursion from the same model are 2.3 for ^{7}Be and ^{36}Cl, 2.2 for ^{14}C and ^{22}Na. Considering the other two models, the Laschamps' increase in ^{10}Be is 1.8 and 2.1 from the GGF100k and LSMOD.2, respectively. Moreover, the variations in production rates predicted by the paleomagnetic field models agree well with the actual measurements from Greenland ice cores, and marine sediments that show a doubling of production rates during the Laschamps excursion (e.g., Simon et al., 2020).

Regarding the hemispheric asymmetry, we discussed this finding in view of different timescales and from several paleomagnetic field models. Chu et al. (2022) showed a systematic asymmetry between the Northern and Southern Hemispheres in terms of the cutoff rigidity, from 1965 to the present, including a faster rate of change in the Southern Hemisphere. Gao et al. (2022b) demonstrated a significant hemispherical asymmetry in the cutoff rigidity over the past 100 ka. This asymmetric shielding consequently propagates to asymmetry in the production rates in the Northern versus Southern Hemisphere. Interestingly, this is observed on all analyzed timescales, from the modern-day, over the Holocene, the geomagnetic excursions, to the past 100 ka. Considering the uneven data distribution, with more paleomagnetic data in the Northern Hemisphere, the question arises if the hemispheric asymmetry is due to the sampling bias. Tests that have been carried out on the Holocene and 100 k models by flipping the data locations available in the Northern and Southern Hemispheres showed that the hemispherical asymmetry is robust and not an artifact of the underlying data distribution (Constable et al., 2016; Panovska et al., 2018). From the point of view of spherical harmonic models, the persistent axial quadrupole term (g_2^0) contributes significantly to the time-averaged geomagnetic field on all timescales (e.g., Panovska et al., 2019), and it also plays a role in the observed asymmetry. The origin of this North/South Hemispheric asymmetry lies within the source of the geomagnetic field, and it is a topic that requires further research (Constable et al., 2016). The dynamics of the lower mantle, core-mantle boundary, inner core, and their coupling may provide clues for resolving this question. Note that the presented estimates are based on only the internal magnetic field, and do not consider the external field—the magnetosphere formed as the dynamic interface between the geomagnetic and interplanetary magnetic fields (e.g., Pulkkinen, 2007). Numerical results show that considering the magnetospheric current system improves the agreement between theoretical and observed cutoff rigidity (e.g., Smart et al., 1969). During the periods of the dipole-dominated geomagnetic field, the contribution of the quiet magnetosphere to the cutoff rigidities is small (Kudela & Usoskin, 2004; Nevalainen et al., 2013), but it may become significant during periods of a weak dipole field. Including the paleomagnetosphere in the cutoff rigidity calculation will affect the production through changes in the shielding against particles of cosmic (and solar) origin (e.g., Glassmeier & Vogt, 2010; Gong et al., 2022; Stadelmann et al., 2010). For space weather applications, cutoff rigidities at different altitudes are required, and scaling them assuming dipolar approximations introduces significant errors, especially during geomagnetic storm times (Kress et al., 2015). Clearly, for consistent results, a realistic magnetosphere corresponding to the time-varying internal geomagnetic field needs to be implemented with a full physical model that remains beyond the framework of this study.

Also, we have used a single average GCR spectrum for these estimates, while the effect of solar variability is not explored here in depth. In addition, possible effects of solar energetic particles on CNPRs especially extreme solar events (e.g., Cliver et al., 2022; Mekhaldi et al., 2021) can also be important. Furthermore, although a constant spectrum over the past 100 ka period is a valid assumption as the spectrum is considered to be stable over this time (e.g., Beer et al., 2012), some variations may affect the production rate results. All these more detailed considerations will be explored in forthcoming works.

This study focuses on the production of meteoric cosmogenic nuclides throughout the multi-millennial timescale, leaving aside effects of the long-term, global geomagnetic field models on in situ nuclide production rates. Both types of nuclides (meteoric and in situ) are widely used as proxies of the past geomagnetic field and solar variability, tracers of Earth surface processes, and as chronological tools (e.g., Clow et al., 2020; Simon et al., 2020; Willenbring & von Blanckenburg, 2010). Other nuclides can be considered as well, for instance, ^{3}H (Poluianov et al., 2020), which is widely used as a tracer of atmospheric and hydrological circulation.

Data Availability Statement

The cosmogenic nuclide production rates presented here are available in the EarthRef.org Digital Archive (ERDA) at https://earthref.org/ERDA/2543/. The cutoff rigidities are analyzed and presented in Gao et al. (2022a, 2022b), available online at https://earthref.org/ERDA/2498/ and https://earthref.org/ERDA/2521/. The yield functions of cosmogenic nuclides are available in the supplementary material of Poluianov et al. (2016).

Acknowledgments

S. Panovska gratefully acknowledges the Discovery Fellowship at the GFZ Potsdam, Germany and the support from the Center of Excellence ReSoLVE (University of Oulu) for the research stay at the University of Oulu, Finland. J. Gao acknowledges financial support from China Scholarship Council (202004910583). The University of Oulu team acknowledges support from the Academy of Finland, project GERACLIS Grant 354280 and QUASARE Grant 330064, and the UO grant SARPEDON. We would like to thank Petr Pisoft for providing the tropopause heights from the JRA55 reanalysis data over the period 1960–2018. We thank Florian Adolphi for providing the Antarctic data, and Raimund Muscheler for Greenland data. Nathaniel Lifton and one anonymous reviewer are greatly acknowledged for their helpful suggestions to improve the paper.

References

Adolphi, F., Ramsey, C. B., Erhardt, T., Edwards, R. L., Cheng, H., Turney, C. S. M., et al. (2018). Connecting the Greenland ice-core and U/Th timescales via cosmogenic radionuclides: Testing the synchroneity of Dansgaard–Oeschger events. *Climate of the Past*, *14*(11), 1755–1781. https://doi.org/10.5194/cp-14-1755-2018

Alken, P., Thébault, E., Beggan, C. D., Amit, H., Aubert, J., Baerenzung, J., et al. (2021). International geomagnetic reference field: The thirteenth generation. *Earth Planets and Space*, *73*(49), 49. https://doi.org/10.1186/s40623-020-01288-x

Asvestari, E., Gil, A., Kovaltsov, G. A., & Usoskin, I. G. (2017). Neutron monitors and cosmogenic isotopes as cosmic ray energy—Integration detectors: Effective yield functions, effective energy, and its dependence on the local interstellar spectrum. *Journal of Geophysical Research: Space Physics*, *122*(10), 9790–9802. https://doi.org/10.1002/2017JA024469

Aubert, J., Finlay, C. C., & Fournier, A. (2013). Bottom-up control of geomagnetic secular variation by the Earth's inner core. *Nature*, *502*(7470), 219–223. https://doi.org/10.1038/nature12574

Balco, G., Stone, J. O., Lifton, N. A., & Dunai, T. J. (2008). A complete and easily accessible means of calculating surface exposure ages or erosion rates from ^{10}Be and ^{26}Al measurements. *Quaternary Geochronology*, *3*, 174–195. https://doi.org/10.1016/j.quageo.2007.12.001

Beer, J., Blinov, A., Bonani, G., Finkel, R. C., Hofmann, H. J., Lehmann, B., et al. (1990). Use of ^{10}Be in polar ice to trace the 11-year cycle of solar activity. *Nature*, *347*(6289), 164–166. https://doi.org/10.1038/347164a0

Beer, J., McCracken, K. G., & von Steiger, R. (2012). *Cosmogenic radionuclides: Theory and applications in the terrestrial and space environments*. Springer. https://doi.org/10.1007/978-3-642-14651-0

Bourlès, D. L., Raisbeck, G. M., & Yiou, F. (1989). ^{10}Be and ^{9}Be in marine sediments and their potential for dating. *Geochimica et Cosmochimica Acta*, *53*(2), 443–452. https://doi.org/10.1016/j.quascirev.2016.03.027

Brown, M. C., Korte, M., Holme, R., Wardinski, I., & Gunnarson, S. (2018). Earth's magnetic field is probably not reversing. *Proceedings of the National Academy of Sciences*, *115*(20), 5111–5116. https://doi.org/10.1073/pnas.1722110115

Caballero-Lopez, R. A., & Moraal, H. (2004). Limitations of the force field equation to describe cosmic ray modulation. *Journal of Geophysical Research*, *109*(A1), A01101. https://doi.org/10.1029/2003JA010098

Carcaillet, J., Bourlès, D. L., Thouveny, N., & Arnold, M. (2004). A high resolution authigenic ^{10}Be/^{9}Be record of geomagnetic moment variations over the last 300 ka from sedimentary cores of the Portuguese margin. *Earth and Planetary Science Letters*, *219*(3–4), 397–412. https://doi.org/10.1016/S0012-821X(03)00702-7

Castagnoli, G., & Lal, D. (1980). Solar modulation effects in terrestrial production of Carbon-14. *Radiocarbon*, *22*(2), 133–158. https://doi.org/10.1017/s0033822200009413

Christl, M., Lippold, J., Steinhilber, F., Bernsdorff, F., & Mangini, A. (2010). Reconstruction of global ^{10}Be production over the past 250 ka from highly accumulating Atlantic drift sediments. *Quaternary Science Reviews*, *29*(19–20), 2663–2672. https://doi.org/10.1016/j.quascirev.2010.06.017

Chu, W., Yang, Y., Xu, S., Qin, G., Huang, J., Zeren, Z., & Shen, X. (2022). Study on long-term variation characteristics of geomagnetic cutoff rigidities of energetic protons caused by long-term variation of geomagnetic field. *Frontiers in Earth Science*, *10*. https://doi.org/10.3389/feart.2022.818788

Cliver, E. W., Schrijver, C. J., Shibata, K., & Usoskin, I. G. (2022). Extreme solar events. *Living Reviews in Solar Physics*, *19*(1), 2. https://doi.org/10.1007/s41116-022-00033-8

Clow, T., Willenbring, J. K., Schaller, M., Blum, J. D., Christl, M., Kubik, P. W., & von Blanckenburg, F. (2020). Calibrating a long-term meteoric ^{10}Be delivery rate into eroding western US glacial deposits by comparing meteoric and in situ produced ^{10}Be depth profiles. *Geochronology*, *2*, 411–423. https://doi.org/10.5194/gchron-2-411-2020

Constable, C. G., & Korte, M. (2015). Centennial-to millennial-scale geomagnetic field variations. In G. Schubert (Ed.), *Treatise on geophysics* (2nd ed., pp. 309–341). Elsevier. https://doi.org/10.1016/B978-0-444-53802-4.00103-2

Constable, C. G., Korte, M., & Panovska, S. (2016). Persistent high paleosecular variation activity in southern hemisphere for at least 10 000 years. *Earth and Planetary Science Letters*, *453*, 78–86. https://doi.org/10.1016/j.epsl.2016.08.015

Cooke, D. J., Humble, J. E., Shea, M. A., Smart, D. F., Lund, N., Rasmussen, I. L., et al. (1991). On cosmic-ray cut-off terminology. *Il Nuovo Cimento C*, *14*(3), 213–234. https://doi.org/10.1007/bf02509357

Elsasser, W., Ney, E. P., & Winckler, J. R. (1956). Cosmic ray intensity and geomagnetism. *Nature*, *178*(4544), 1226–1227. https://doi.org/10.1038/1781226a0

Frank, M., Schwarz, B., Baumann, S., Kubik, P. W., Suter, M., & Mangini, A. (1997). A 200 kyr record of cosmogenic radionuclide production rate and geomagnetic field intensity from ^{10}Be in globally stacked deep-sea sediments. *Earth and Planetary Science Letters*, *149*(1–4), 121–129. https://doi.org/10.1016/s0012-821x(97)00070-8

Gao, J., Korte, M., Panovska, S., Rong, Z., & Wei, Y. (2022a). Effects of the Laschamps excursion on geomagnetic cutoff rigidities. *Geochemistry, Geophysics, Geosystems*, *23*(2), e2021GC010261. https://doi.org/10.1029/2021GC010261

Gao, J., Korte, M., Panovska, S., Rong, Z., & Wei, Y. (2022b). Geomagnetic field shielding over the last one hundred thousand years. *Journal of Space Weather and Space Climate*, *12*, 31. https://doi.org/10.1051/swsc/2022027

Glassmeier, K., & Vogt, J. (2010). Magnetic polarity transitions and biospheric effects. *Space Science Reviews*, *155*(1–4), 387–410. https://doi.org/10.1007/s11214-010-9659-6

Golubenko, K., Rozanov, E., Kovaltsov, G., & Usoskin, I. (2022). Zonal mean distribution of cosmogenic isotope (^{7}Be, ^{10}Be, ^{14}C, and ^{36}Cl) production in stratosphere and troposphere. *Journal of Geophysical Research: Atmospheres*, *127*(16), e36726. https://doi.org/10.1029/2022JD036726

Gong, F., Yu, Y., Cao, J., Wei, Y., Gao, J., Li, H., et al. (2022). Simulating the solar wind-magnetosphere interaction during the Matuyama-Brunhes paleomagnetic reversal. *Geophysical Research Letters*, *49*(3), e2021GL097340. https://doi.org/10.1029/2021GL097340

Heikkilä, U., Beer, J., & Feichter, J. (2008). Modeling cosmogenic radionuclides ^{10}Be and ^{7}Be during the Maunder Minimum using the ECHAM5-HAM general circulation model. *Atmospheric Chemistry and Physics*, *8*(10), 2797–2809. https://doi.org/10.5194/acp-8-2797-2008

Heikkilä, U., Beer, J., & Feichter, J. (2009). Meridional transport and deposition of atmospheric ^{10}Be. *Atmospheric Chemistry and Physics*, *9*(2), 515–527. https://doi.org/10.5194/acp-9-515-2009

Heikkilä, U., & von Blanckenburg, F. (2015). The global distribution of Holocene meteoric ^{10}Be fluxes from atmospheric models. In *Distribution maps for terrestrial Earth's surface applications*. GFZ Data Services. https://doi.org/10.5880/GFZ.3.4.2015.001

Jackson, A., & Finlay, C. C. (2015). Geomagnetic secular variation and its application to the core. In G. Schubert (Ed.), *Treatise on geophysics* (2nd ed., pp. 137–184). Elsevier. https://doi.org/10.1016/B978-0-444-53802-4.00099-3

Johnson, C. L., & McFadden, P. (2015). The time-averaged field and paleosecular variation. In G. Schubert (Ed.), *Treatise on geophysics* (Vol. 5, pp. 385–417). Elsevier. https://doi.org/10.1016/B978-0-444-53802-4.00105-6

Köhler, P., Adolphi, F., Butzin, M., & Muscheler, R. (2022). Toward reconciling radiocarbon production rates with carbon cycle changes of the last 55,000 years. *Paleoceanography and Paleoclimatology*, *37*(2), e2021PA004314. https://doi.org/10.1029/2021PA004314

Koldobskiy, S. A., Bindi, V., Corti, C., Kovaltsov, G. A., & Usoskin, I. G. (2019). Validation of the neutron monitor yield function using data from AMS-02 experiment, 2011–2017. *Journal of Geophysical Research: Space Physics*, *124*(4), 2367–2379. https://doi.org/10.1029/2018JA026340

Korte, M., Brown, M. C., Panovska, S., & Wardinski, I. (2019). Robust characteristics of the Laschamps and Mono Lake geomagnetic excursions: Results from global field models. *Frontiers in Earth Science*, *7*. https://doi.org/10.3389/feart.2019.00086

Kovaltsov, G. A., Mishev, A., & Usoskin, I. G. (2012). A new model of cosmogenic production of radiocarbon ^{14}C in the atmosphere. *Earth and Planetary Science Letters*, *337*, 114–120. https://doi.org/10.1016/j.epsl.2012.05.036

Kovaltsov, G. A., & Usoskin, I. G. (2010). A new 3D numerical model of cosmogenic nuclide ^{10}Be production in the atmosphere. *Earth and Planetary Science Letters*, *291*(1–4), 182–188. https://doi.org/10.1016/j.epsl.2010.01.011

Kress, B. T., Hudson, M. K., Selesnick, R. S., Mertens, C. J., & Engel, M. (2015). Modeling geomagnetic cutoffs for space weather applications. *Journal of Geophysical Research: Space Physics*, *120*(7), 5694–5702. https://doi.org/10.1002/2014JA020899

Kudela, K., & Usoskin, I. G. (2004). On magnetospheric transmissivity of cosmic rays. *Czechoslovak Journal of Physics*, *54*(2), 239–254. https://doi.org/10.1023/B:CJOP.0000014405.61950.e5

Lal, D., & Peters, B. (1967). Cosmic ray produced radioactivity on the Earth. In S. Flügge (Ed.), *Handbuch für Physik* (pp. 551–612). Springer.

Leonhardt, R., Fabian, K., Winklhofer, M., Ferk, A., Laj, C., & Kissel, C. (2009). Geomagnetic field evolution during the Laschamp excursion. *Earth and Planetary Science Letters*, *278*(1–2), 87–95. https://doi.org/10.1016/j.epsl.2008.11.028

Lifton, N., Sato, T., & Dunai, T. J. (2014). Scaling *in situ* cosmogenic nuclide production rates using analytical approximations to atmospheric cosmic-ray fluxes. *Earth and Planetary Science Letters*, *386*, 149–160. https://doi.org/10.1016/j.epsl.2013.10.052

Lifton, N., Smart, D., & Shea, M. (2008). Scaling time-integrated in situ cosmogenic nuclide production rates using a continuous geomagnetic model. *Earth and Planetary Science Letters*, *268*(1–2), 190–201. https://doi.org/10.1016/j.epsl.2008.01.021

Masarik, J., & Beer, J. (1999). Simulation of particle fluxes and cosmogenic nuclide production in the Earth's atmosphere. *Journal of Geophysical Research*, *104*(D10), 12009–12111. https://doi.org/10.1029/1998JD200091

Masarik, J., & Beer, J. (2009). An updated simulation of particle fluxes and cosmogenic nuclide production in the Earth's atmosphere. *Journal of Geophysical Research*, *114*(D11103), D11103. https://doi.org/10.1029/2008JD010557

Mekhaldi, F., Adolphi, F., Herbst, K., & Muscheler, R. (2021). The signal of solar storms embedded in cosmogenic radionuclides: Detectability and uncertainties. *Journal of Geophysical Research: Space Physics*, *126*(8), e2021JA029351. https://doi.org/10.1029/2021JA029351

Mishev, A. L., Poluianov, S. V., & Usoskin, I. (2017). Assessment of spectral and angular characteristics of sub-GLE events using the global neutron monitor network. *Journal of Space Weather and Space Climate*, *7*(27), A28. https://doi.org/10.1051/swsc/2017026

Muscheler, R., Beer, J., Wagner, G., Laj, C., Kissel, C., Raisbeck, G. M., et al. (2004). Changes in the carbon cycle during the last deglaciation as indicated by the comparison of ^{10}Be and ^{14}C records. *Earth and Planetary Science Letters*, *219*(3–4), 325–340. https://doi.org/10.1016/s0012-821x(03)00722-2

National Oceanic and Atmospheric Administration. (1976). *U.S. standard atmosphere*. US Government Printing Office.

Nevalainen, J., Usoskin, I. G., & Mishev, A. (2013). Eccentric dipole approximation of the geomagnetic field: Application to cosmic ray computations. *Advances in Space Research*, *52*(1), 22–29. https://doi.org/10.1016/j.asr.2013.02.020

Nilsson, A., Suttie, N., Stoner, J., & Muscheler, R. (2022). Recurrent ancient geomagnetic field anomalies shed light on future evolution of the South Atlantic Anomaly. *Proceedings of the National Academy of Sciences*, *119*(24), e2200749119. https://doi.org/10.1073/pnas.2200749119

Panovska, S., Constable, C. G., & Korte, M. (2018). Extending global continuous geomagnetic field reconstructions on timescales beyond human civilization. *Geochemistry, Geophysics, Geosystems*, *19*(12), 4757–4772. https://doi.org/10.1029/2018GC007966

Panovska, S., Korte, M., & Constable, C. G. (2019). One hundred thousand years of geomagnetic field evolution. *Reviews of Geophysics*, *57*(4), 1289–1337. https://doi.org/10.1029/2019RG000656

Panovska, S., Korte, M., Finlay, C. C., & Constable, C. G. (2015). Limitations in paleomagnetic data and modelling techniques and their impact on Holocene geomagnetic field models. *Geophysical Journal International*, *202*(1), 402–418. https://doi.org/10.1093/gji/ggv137

Panovska, S., Korte, M., Liu, J., & Nowaczyk, N. R. (2021). Global evolution and dynamics of the geomagnetic field in the 15–70 kyr period based on selected paleomagnetic sediment records. *Journal of Geophysical Research: Solid Earth*, *126*(12), e2021JB022681. https://doi.org/10.1029/2021JB022681

Pavón-Carrasco, F. J., Osete, M. L., Torta, J. M., & De Santis, A. (2014). A geomagnetic field model for the Holocene based on archaeomagnetic and lava flow data. *Earth and Planetary Science Letters*, *388*, 98–109. https://doi.org/10.1016/j.epsl.2013.11.046

Pisoft, P., Sacha, P., Polvani, L. M., Añel, J. A., Huszar, P., Jacobi, C., et al. (2021). Stratospheric contraction caused by increasing greenhouse gases. *Environmental Research Letters*, *16*(6), 140–152. https://doi.org/10.1088/1748-9326/abfe2b

Poluianov, S. V., Kovaltsov, G. A., Mishev, A. L., & Usoskin, I. G. (2016). Production of cosmogenic isotopes ^{7}Be, ^{10}Be, ^{14}C, ^{22}Na, and ^{36}Cl in the atmosphere: Altitudinal profiles of yield functions. *Journal of Geophysical Research: Atmospheres*, *121*(13), 8125–8136. https://doi.org/10.1002/2016JD025034

Poluianov, S. V., Kovaltsov, G. A., & Usoskin, I. G. (2018). Solar energetic particles and galactic cosmic rays over millions of years as inferred from data on cosmogenic ^{26}Al in lunar samples. *Astronomy & Astrophysics*, *618*(A96), 1–9. https://doi.org/10.1051/0004-6361/201833561

Poluianov, S. V., Kovaltsov, G. A., & Usoskin, I. G. (2020). A new full 3-D model of cosmogenic tritium ^{3}H production in the atmosphere (CRAC:3H). *Journal of Geophysical Research: Atmospheres*, *125*(18), e2020JD033147. https://doi.org/10.1029/2020JD033147

Poluianov, S. V., Usoskin, I. G., & Kovaltsov, G. A. (2014). Cosmogenic isotope variability during the Maunder Minimum: Normal 11-year cycles are expected. *Solar Physics*, *289*(12), 4701–4709. https://doi.org/10.1007/s11207-014-0587-6

Potgieter, M. S. (2013). Solar modulation of cosmic rays. *Living Reviews in Solar Physics*, *10*, 3. https://doi.org/10.12942/lrsp-2013-3

Pulkkinen, T. (2007). Space weather: Terrestrial perspective. *Living Reviews in Solar Physics*, *4*, 1. https://doi.org/10.12942/lrsp-2007-1

Raisbeck, G. M., Cauquoin, A., Jouzel, J., Landais, A., Petit, J., Lipenkov, V. Y., et al. (2017). An improved north–south synchronization of ice core records around the 41 kyr ^{10}Be peak. *Climate of the Past*, *13*(3), 217–229. https://doi.org/10.5194/cp-13-217-2017

Schanner, M., Korte, M., & Holschneider, M. (2022). ArchKalmag14k: A Kalman-filter based global geomagnetic model for the Holocene. *Journal of Geophysical Research: Solid Earth*, *127*(2), e2021JB023166. https://doi.org/10.1029/2021JB023166

Shea, M., Smart, D., & McCracken, K. (1965). A study of vertical cutoff rigidities using sixth degree simulations of the geomagnetic field. *Journal of Geophysical Research*, *70*(17), 4117–4130. https://doi.org/10.1029/jz070i017p04117

Simon, Q., Thouveny, N., Bourlès, D. L., Bassinot, F., Savranskaia, T., Valet, J., & Team, A. (2018). Increased production of cosmogenic ^{10}Be recorded in oceanic sediment sequences: Information on the age, duration, and amplitude of the geomagnetic dipole moment minimum over the Matuyama-Brunhes transition. *Earth and Planetary Science Letters*, *489*, 191–202. https://doi.org/10.1016/j.epsl.2018.02.036

Simon, Q., Thouveny, N., Bourlès, D. L., Valet, J.-P., & Bassinot, F. (2020). Cosmogenic ^{10}Be production records reveal dynamics of geomagnetic dipole moment (GDM) over the Laschamp excursion (20-60 ka). *Earth and Planetary Science Letters*, *550*, 116547. https://doi.org/10.1016/j.epsl.2020.116547

Simon, Q., Thouveny, N., Bourlès, D. L., Valet, J.-P., Bassinot, F., Ménabréaz, L., et al. (2016). Authigenic ^{10}Be/^{9}Be ratio signatures of the cosmogenic nuclide production linked to geomagnetic dipole moment variation since the Brunhes/Matuyama boundary. *Journal of Geophysical Research: Solid Earth*, *121*(11), 7716–7741. https://doi.org/10.1002/2016JB013335

Smart, D. F., & Shea, M. A. (2009). Fifty years of progress in geomagnetic cutoff rigidity determinations. *Advances in Space Research*, *44*(10), 1107–1123. https://doi.org/10.1016/j.asr.2009.07.005

Smart, D. F., Shea, M. A., & Flückiger, E. O. (2000). Magnetospheric models and trajectory computations. *Space Science Reviews*, *93*(1/2), 305–333. https://doi.org/10.1023/a:1026556831199

Smart, D. F., Shea, M. A., & Gall, R. (1969). The daily variation of trajectory-derived high-latitude cutoff rigidities in a model magnetosphere. *Journal of Geophysical Research*, *74*(19), 4731–4738. https://doi.org/10.1029/JA074i019p04731

Solanki, S. K., Usoskin, I. G., Kromer, B., Schüssler, M., & Beer, J. (2004). Unusual activity of the Sun during recent decades compared to the previous 11,000 years. *Nature*, *431*(7012), 1084–1087. https://doi.org/10.1038/nature02995

Stadelmann, A., Vogt, J., Glassmeier, K., Kallenrode, M., & Voigt, G. (2010). Cosmic ray and solar energetic particle flux in paleomagnetospheres. *Earth Planets and Space*, *62*(3), 333–345. https://doi.org/10.5047/eps.2009.10.002

Steinhilber, F., Abreu, J. A., Beer, J., Brunner, I., Christl, M., Fischer, H., et al. (2012). 9,400 years of cosmic radiation and solar activity from ice cores and tree rings. *Proceedings of the National Academy of Sciences*, *109*(16), 5967–5971. https://doi.org/10.1073/pnas.1118965109

Størmer, C. (1955). *The polar aurora*. Oxford University Press.

Usoskin, I. G. (2023). A history of solar activity over millennia. *Living Reviews in Solar Physics*, *20*(1), 2. https://doi.org/10.1007/s41116-023-00036-z

Usoskin, I. G., Alanko-Huotari, K., Kovaltsov, G. A., & Mursula, K. (2005). Heliospheric modulation of cosmic rays: Monthly reconstruction for 1951–2004. *Journal of Geophysical Research*, *110*(A12), A12108. https://doi.org/10.1029/2005JA011250

Usoskin, I. G., Gallet, Y., Lopes, F., Kovaltsov, G. A., & Hulot, G. (2016). Solar activity during the Holocene: The Hallstatt cycle and its consequence for grand minima and maxima. *Astronomy & Astrophysics*, *587*(A150), 1–10. https://doi.org/10.1051/0004-6361/201527295

Usoskin, I. G., Gil, A., Kovaltsov, G. A., Mishev, A. L., & Mikhailov, V. V. (2017). Heliospheric modulation of cosmic rays during the neutron monitor era: Calibration using PAMELA data for 2006–2010. *Journal of Geophysical Research: Space Physics*, *122*(4), 3875–3887. https://doi.org/10.1002/2016JA023819

Usoskin, I. G., Solanki, S. K., & Korte, M. (2006). Solar activity reconstructed over the last 7000 years: The influence of geomagnetic field changes. *Geophysical Research Letters*, *33*(8), L08103. https://doi.org/10.1029/2006GL025921

Usoskin, I. G., Solanki, S. K., Krivova, N., Hofer, B., Kovaltsov, G. A., Wacker, L., et al. (2021). Solar cyclic activity over the last millennium reconstructed from annual ^{14}C data. *Astronomy & Astrophysics*, *649*, A141. https://doi.org/10.1051/0004-6361/202140711

Vogt, J., & Glassmeier, K. (2001). Modelling the paleomagnetosphere: Strategy and first results. *Advances in Space Research*, *28*(6), 863–868. https://doi.org/10.1016/s0273-1177(01)00504-x

Vos, E. E., & Potgieter, M. S. (2015). New modeling of galactic proton modulation during the minimum of solar cycle 23/24. *The Astrophysical Journal*, *815*(2), 119. https://doi.org/10.1088/0004-637X/815/2/119

Willenbring, J. K., & von Blanckenburg, F. (2010). Meteoric cosmogenic Beryllium-10 adsorbed to river sediment and soil: Applications for Earth-surface dynamics. *Earth-Science Reviews*, *98*(1–2), 105–122. https://doi.org/10.1016/j.earscirev.2009.10.008

Wu, C. J., Usoskin, I. G., Krivova, N., Kovaltsov, G., Baroni, M., Bard, E., & Solanki, S. K. (2018). Solar activity over nine millennia: A consistent multi-proxy reconstruction. *Astronomy & Astrophysics*, *615*, A93. https://doi.org/10.1051/0004-6361/201731892

Zheng, M., Sturevik-Storm, A., Nilsson, A., Adolphi, F., Aldahan, A., Possnert, G., & Muscheler, R. (2021). Geomagnetic dipole moment variations for the last glacial period inferred from cosmogenic radionuclides in Greenland ice cores via disentangling the climate and production signals. *Quaternary Science Reviews*, *258*, 106881. https://doi.org/10.1016/j.quascirev.2021.106881